Received: 25 February 2017 | Revised: 22 April 2017 | Accepted: 19 May 2017

DOI: 10.1002/jbio.201700055

Journal of BIOPHOTONICS

FULL ARTICLE

K-distribution three-dimensional mapping of biological tissues in optical coherence tomography

Mitsuro Sugita[1*] | Robert A. Brown[2] | Ivan Popov[1] | Alex Vitkin[1,3,4]

[1]Department of Medical Biophysics, University of Toronto, Toronto, Canada

[2]Brain Imaging Centre, Montreal Neurological Institute, McGill University, Montreal, Canada

[3]Department of Radiation Oncology, University of Toronto, Toronto, Canada

[4]Division of Biophysics and Bioimaging, Ontario Cancer Institute/University Health Network, Toronto, Canada

***Correspondence**
Department of Medical Biophysics, University of Toronto, Toronto Medical Discovery Tower, 101 College Street, Toronto, Ontario M5G 1L7, Canada.
Email: mitsuro.sugita@uhnres.utoronto.ca

Funding information
Canadian Institutes of Health Research, Grant/Award number: 126172; Ministry of Education and Science of the Russian Federation, Grant/Award number: 14.B25.31.0015; Natural Sciences and Engineering Research Council of Canada, Grant/Award number: J365581-09.

Probability density function (PDF) analysis with K-distribution model of optical coherence tomography (OCT) intensity signals has previously yielded a good representation of the average number of scatterers in a coherence volume for microspheres-in-water systems, and has shown initial promise for biological tissue characterization. In this work, we extend these previous findings, based on single point M-mode or two-dimenstional slice analysis, to full three-dimensional (3D) imaging maps of the shape parameter α of the K-distribution PDF. After selecting a suitably sized 3D evaluation window, and verifying methodology in phantoms, the resultant parametric α images obtained in different animal tissues (rat liver and brain) show new contrasting ability not seen in conventional OCT intensity images.

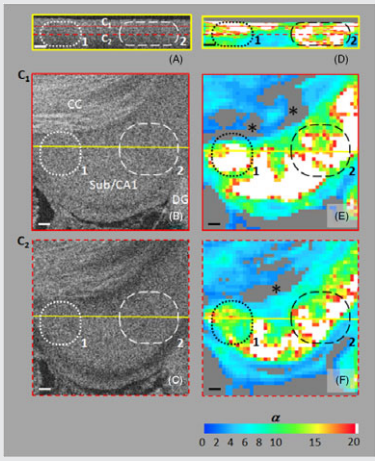

KEYWORDS
light scattering, optical coherence tomography, statistical optics, tissue imaging

1 | INTRODUCTION

In optical investigations of turbid media, the K-distribution has been employed to represent the non-Gaussian optical scattering regime in both theoretical and experimental studies [1–6] Among the variety of optical measurement and analysis methodologies with the K-distribution model, its application to optical coherence tomography (OCT) analysis of the intensity probability density function (PDF) has yielded successful estimation of the number of scatterers within the coherence volume (eg, in the microspheres-in-water phantom system, ranging from a few to >50) [7, 8]. Initial possibilities for biological tissue characterization have also been demonstrated in in vivo human skin and nail [8].

The K-distribution analysis in the previous studies of OCT intensity PDFs was processed with pixel sampling by either single point M-mode or in two-dimensional slices. These limited-dimensionality approaches are unlikely to provide appropriate fields of view (FOV) and spatial resolutions for full three-dimensional (3D) tissue imaging, for example, as needed to differentiate localized regions of tissue pathology. In order to achieve reasonable volumetric spatial resolution, it is necessary to introduce a 3D evaluation window that samples the imaged tissue volume and has a reasonably small dimension (eg, <0.1 mm^3), yet contains enough voxels and independent speckles to maintain good statistics for the PDF analysis to furnish robust estimates of the K-distribution shape parameter α.

In this paper, we thus present a first demonstration of 3D α-mapping in ex vivo biological tissues, with a suitably selected 3D volumetric sliding evaluation window. Studies in approximately homogeneous (rat liver) and heterogeneous (rat brain) tissues reveal novel and interesting contrast

not directly visible on OCT structural images. Quantitative linkages of these parametric maps to details of underlying tissue microstructure (the effective number of tissue scatterers in a coherence volume) are also briefly discussed.

2 | MATERIALS AND METHODS

2.1 | Sample preparation

Prior to biological tissue experiments, a control homogenous particles-in-water phantom was examined. Polystyrene microspheres with a diameter of 0.96 μm (Bang Laboratories Inc., Fishers, Indiana) were suspended in deionized water at a concentration of 0.5% solids (1.1×10^{-3} particles per μm^3). A droplet (approximately 5 μL) of the suspension was placed on a 1-mm-thick glass microscope slide and gently covered by another identical slide. The top surface of the flattened droplet contacted the lower surface of the covering slide with a surface area of approximately 10 mm^2. The OCT imaging was conducted through the 1-mm-thick cover slide to avoid effects from tails of strong specular reflection signal, generated at the air–glass interface and extended to the sample depths in OCT A-scans.

As an example of relatively homogeneous biological tissue, we next examined rat liver, excised from healthy rats. Within 30 min of excision, the samples were frozen by liquid nitrogen and stored at −80°C. Prior to the OCT measurements, the samples were thawed at 4°C for 16 h. Similar to the phantom above, liver was placed between two microscope slides for OCT imaging.

Inhomogeneous biological tissue was then investigated. Brain tissue was extracted from healthy rats, then fixed in formalin and sectioned into 0.8-mm-thick slices. The sliced sample was placed in a Petri dish and covered to a depth of 1 mm above the brain slice surface with phosphate buffer solution (for same reasons as phantom and unfixed liver tissue arrangements above).

2.2 | OCT instrumentation, scan protocol and data processing

OCT imaging was conducted by a fiber-based spectral domain OCT described previously [8, 9]. Super-luminescent diodes light source centered at 1320 nm with a bandwidth of 110 nm Full Width at Half Maximum (FWHM) seeded the system. A custom-made spectrometer with a transmission diffraction grating and a line sensor camera (1024-pixel InGaAs photodiode array) was used for the acquisition of the interferograms, performed at 47 kHz. A pair of *xy*-galvo-mirrors followed by 4f-system relay optics (1× magnification) and an objective lens (20 mm focal length) were configured to scan up to a 2 × 2 mm *en face* FOV. The OCT sensitivity was 92 dB at 200 μm depth (in air), and the roll-off was −10 dB/mm. The lateral spot size diameter $2w_1$ was 23 μm (1/e-amplitude width measured). The 1/e-amplitude width of the coherence function $2w_2$ was 9.8 μm in water ($n = 1.32$ at 1300 nm). The maximum imaging depth was 1.5 mm (as per Nyquist limit with the spectrometer pixel resolution = 0.22 nm) and the depth of focus was 420 μm (as per Rayleigh range); the both were calculated for water. The *x-y-z* voxel sizes were (1) $2.0 \times 2.0 \times 0.65$ μm^3 for 1×1 mm^2 *en face* FOV case with 512 × 512 A-scans in (*x*,*y*), and (2) $3.9 \times 3.9 \times 0.65$ μm^3 for 1.5×1.5 mm^2 FOV case (extracted from 2×2 mm^2 *en face* FOV scan with 512 × 512 A-scans in (*x*,*y*); these calculations assumed $n = 1.4$ for tissue. All scanning and sampling conditions ensured oversampling.

The coherence volume of this OCT imager was calculated as $V = \pi^{3/2} \cdot {w_{confocal}}^2 \cdot w_2 = \sim(12\ \mu m)^3$, defined by a volume integral of the 3D Gaussian point spread function (PSF) for OCT signal amplitude [10–12]:

$$PSF(x,y,z) = \exp\left(-\frac{x^2+y^2}{w_{confocal}^2}\right)\exp\left(-\frac{(z-z_0)^2}{{w_2}^2}\right), \quad (1)$$

where $w_{confocal}$ is the 1/e-Gaussian-beam-intensity radius, which is $1/\sqrt{2}$ of the $1/e^2$-intensity (1/e-amplitude) radius w_1. This factor of $1/\sqrt{2}$ (thus factor of 2 for the volume) originates from the confocal setup of the OCT imager in which the overlap integral of the illumination and collection optical mode fields should be taken into account [13–15]; this formulation also corrects our slight inconsistency published previously [7]. For the microspheres-in-water phantom examined here, the average number of particles *N* within the coherence volume *V* was ~1.9.

Signal processing was performed through the following steps. (1) Spectral domain OCT signal processing: wavenumber *k*-linearization and numerical dispersion compensation (second and third orders) for the acquired interferogram, zero-padding (from 1024 to 4096) and inverse Fourier transform; (2) sample surface segmentation and flattening: the surface was detected by OCT intensity change in each B-scan image after median filtering, and then the 3D volume data was reconfigured to have a flat surface; (3) K-distribution fitting: OCT intensity histogram in a 3D sliding evaluation window ($x \times y \times z$: $36 \times 36 \times 72$ or $18 \times 18 \times 72$ voxels—the larger number of pixels in the depth direction is chosen based on the higher axial resolution of OCT) was fitted to the normalized K-distribution PDF expressed as [8]:

$$P_\alpha(I) = \frac{2\alpha}{\Gamma(\alpha)} \cdot (\alpha I)^{(\alpha-1)/2} \cdot K_{\alpha-1}\left(2\sqrt{\alpha I}\right), \quad (2)$$

where $\Gamma(x)$ is the Gamma function, $K_\nu(x)$ is a modified Bessel function of the second kind and α is the shape parameter used for fitting. The 3D evaluation window was moved along either a B-scan or a C-scan (*en face*) plane in

its two dimensions, and the fitting was performed at every 8 pixel step in each direction. The fitted α values were displayed as a color-coded map. Pixels with poor goodness-of-fit (below threshold) were excluded and displayed in a grey color in the α-map. Mean square error (MSE) was used for the goodness-of-fit measure and a threshold for good/poor fit was set empirically at MSE = 3×10^{-7}.

3 | RESULTS AND DISCUSSIONS

The purpose of the initial phantom study was to examine the α-mapping methodology in a homogeneous well-defined scattering system. We thus expect the resultant α maps to be homogeneous, and from the resultant fluctuations we can evaluate the range of random errors. Further, knowing N permits the accuracy assessment of the K-distribution approach through its expected dependence $N = \alpha/2$ [7, 8]. Studies in this control phantom also enable examination of optimal and practical conditions for the size of the 3D evaluation window.

Figure 1 shows results of the microspheres-in-water phantom. The *en face* FOV was 1×1 mm^2 with 512×512 A-scans. As expected, the OCT intensity images and α-maps are overall homogeneous, with no distinct features. The mean ± standard deviation (SD) of α within the B- and C-scans, excluding the poor goodness-of-fit pixels, are 3.9 ± 0.7 (Figure 1E), 4.0 ± 0.6 (Figure 1F) and 4.0 ± 0.8 (Figure 1G). The average number of scattering microspheres in a unit coherence volume is thus predicted

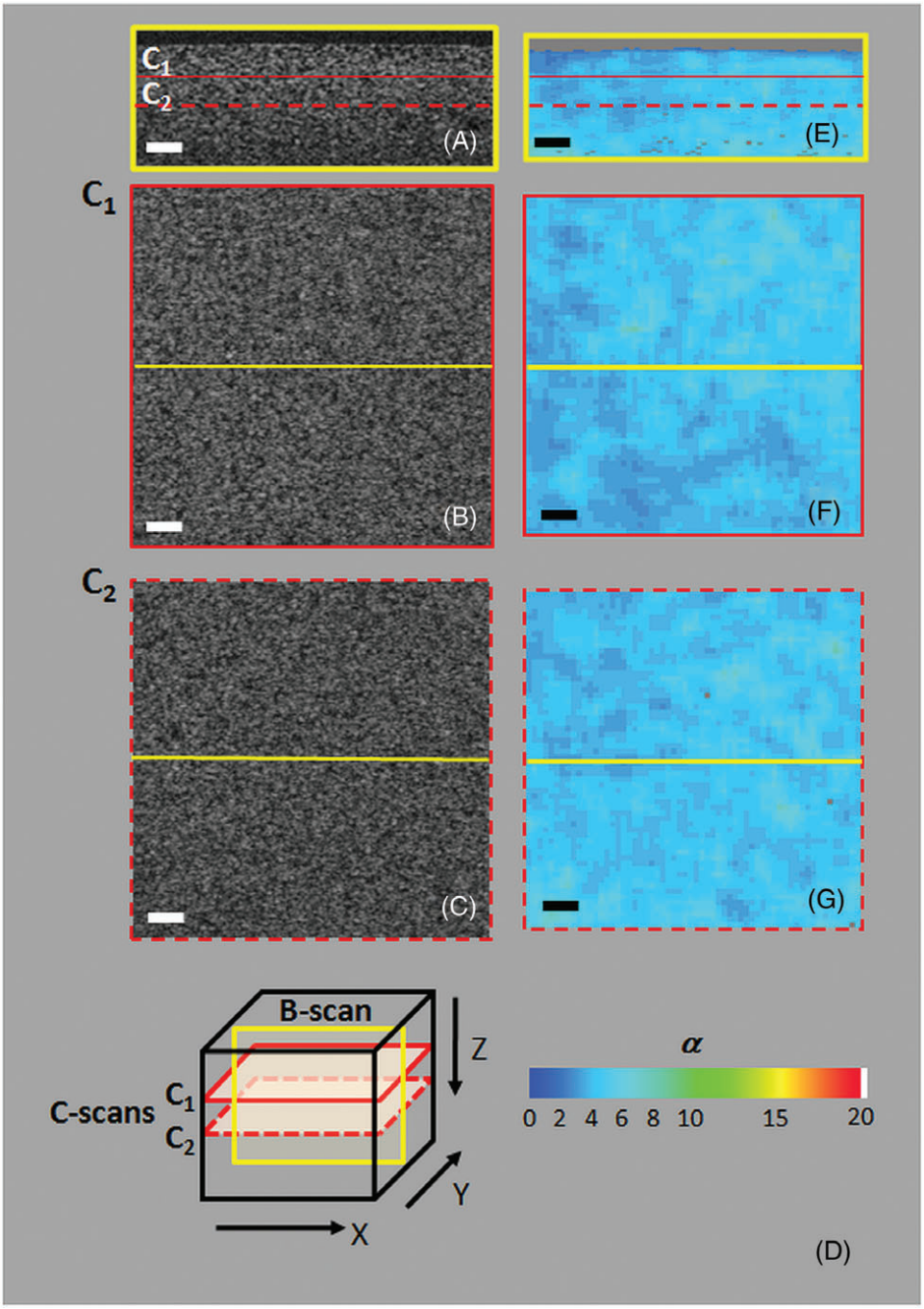

FIGURE 1 Microspheres-in-water phantom results for OCT intensity images and α-maps by the K-distribution fit. Left side: OCT intensity B- and C-mode images. (A) B-mode; (B) C-mode at depth C_1 = 90 μm; (C) C-mode at depth C_2 = 180 μm. (D) Configuration and labeling of the B-scan and C-scan images in 3D volume used in Figures 1–2 and 4. Right side: α-maps. (E) B-mode corresponding to (A); (F) C-mode at depth C_1 corresponding to (B); (G) C-mode at depth C_2 corresponding to (C). Note the relatively homogeneous results centered around α ~ 4 (see text for details). Scale bars: 100 μm

to be $N = \alpha/2 \sim 2.0$, which is in good agreement with the real value $N = 1.9$. The ranges of the resultant α SD values are seen to be <1, suggesting that perhaps K-distribution fitting results with this magnitude of random uncertainty in α are credible and can be reasonably trusted as we move to the unknown tissue systems.

As mentioned previously, the 3D sliding evaluation window should be sufficiently large to contain enough voxels and independent speckles for robust statistical analysis, but not too large as to wash out tissue features and details, yielding poorly resolved α-maps. Comparisons of two 3D window sizes, 36 × 36 × 72-voxels (72 × 72 × 50 μm^3 in water, containing 93 k voxels and ~140–430 speckles [16]; used in Figure 1) and 18 × 18 × 72-voxels (36 × 36 × 50 μm^3, containing 23 k voxels and ~40–110 speckles; data not shown) were performed. The latter is obviously preferable

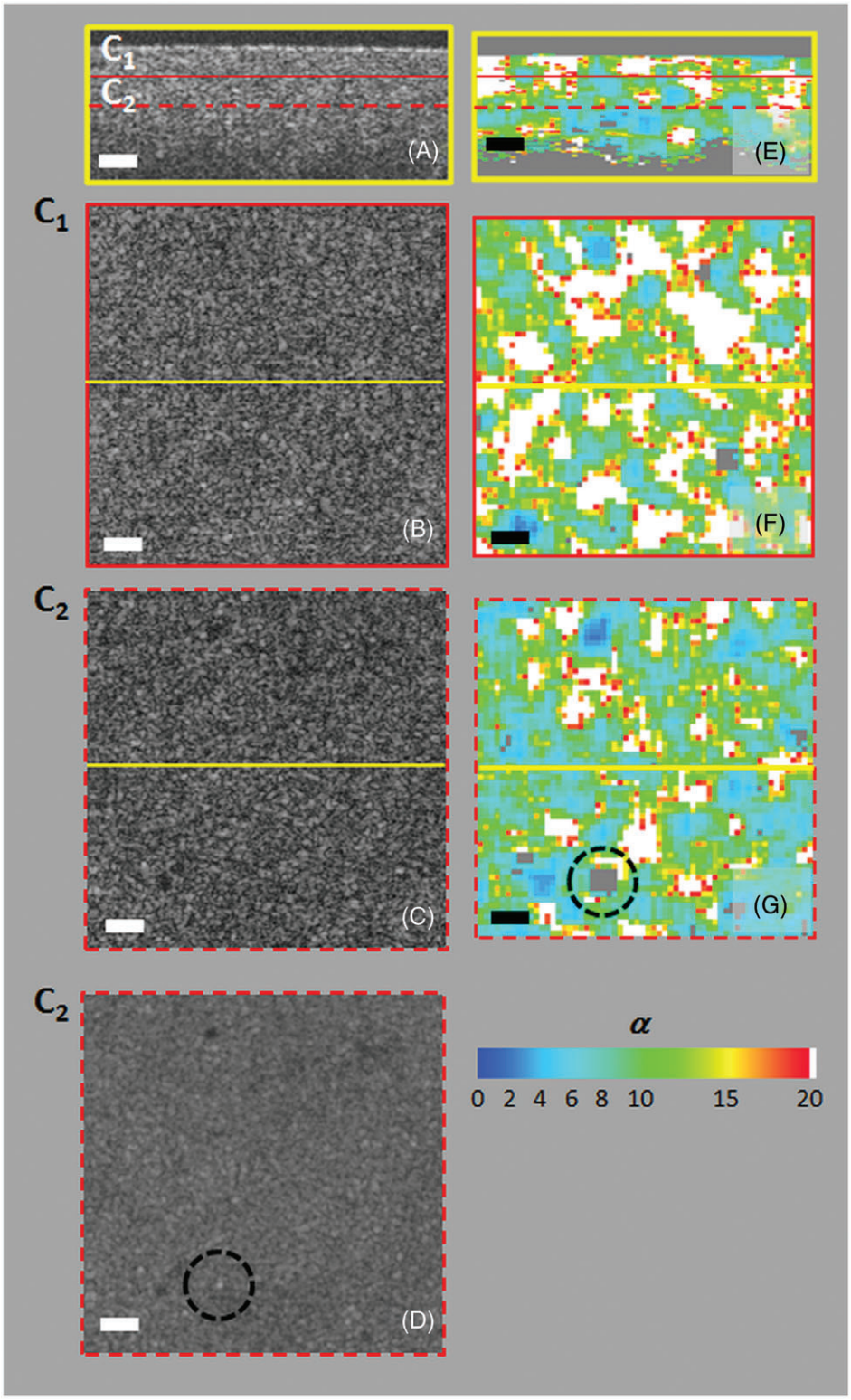

FIGURE 2 OCT intensity images and α-maps by K-distribution fits in rat liver. Left side: OCT intensity B- and C-mode images. (A) B-mode; (B) C-mode at depth C_1 = 85 μm; (C) C-mode at depth C_2 = 170 μm; (D) *en face* averaged intensity projection (72 frame average with the center frame at C_2). Right side: α-maps. (E) B-mode corresponding to (A); (F) C-mode at depth C_1 corresponding to (B); (G) C-mode at depth C_2 corresponding to (C); grey areas indicate the exclusion of the poor goodness-of-fit pixels (MSE > 3×10^{-7}). Scale bars: 100 μm. Regions with high α values (>20, displayed as white) are observed near the sample surface, which are not evident in the corresponding OCT intensity images; their prevalence decreases with depth (compare (F) and (G)). Exclusion of pixels by poor fit is observed at the encircled area in the α-map of (G); this stems from a real structural heterogeneity best seen in the structural image averaged intensity projection in (D)

because of its finer spatial resolution, but its resultant mean ± SD α values were 4.3 ± 1.5, 4.4 ± 1.3 and 4.5 ± 1.6 for the one B-mode and the two C-mode *en face* sections shown in Figure 1. Compared to the above results from the larger 3D evaluation window, we note the degradation in precision (larger SD) and decreased accuracy (larger deviation from the expected "correct" value of α ~ 4); both suggest insufficient/biased statistics of PDF fitting in this smaller number of voxels. Thus, despite the somewhat inferior spatial resolution of the larger 3D evaluation window, its 36 × 36 × 72-voxel condition was used throughout the remainder of this paper.

The rat liver samples were studied as an example of a relatively homogeneous biological tissue. The *en face* FOV was 1 × 1 mm^2 with 512 × 512 A-scans. The OCT intensity images and resultant tissue mapping by K-distribution PDF fitting are shown in Figure 2. In addition to the data in Figure 2, two more rat liver samples, with three sampling locations on each, were subjected to OCT imaging and associated PDF analysis. The derived six α-maps showed similar trends; thus, only one representative liver results summary is shown in Figure 2.

In Figure 2, it is reasonable to similarly expect neither definitive structures nor features in both the OCT tomographs and in the corresponding α-maps. This is indeed borne out for the OCT intensity images (left column of Figure 2). However, in the α-maps, scattered high α value areas exist near the sample surface, typically down to ~150 μm depth (see Figure 2E, and compare Figure 2F,G). Yet significant variations are not evident in the corresponding OCT intensity images. This unexpected contrast in the α-maps is intriguing and may arise from real tissue structural variation and/or optical scattering property heterogeneities in the rat liver sample.

In order to interpret this difference between the OCT intensity images and α-maps, and to determine whether the novel contrast in the latter is real or artefactual, histology was conducted. The sample was fixed in formalin immediately after the OCT imaging for 72 h, embedded in paraffin and sectioned for hemotoxylin and eosin staining and microscopy at approximately the same position along the OCT B-scan (Figure 2A).

Figure 3A shows the resultant histology slice, compared with the corresponding OCT α-map (Figure 3B, reproduced from Figure 2E). In the top region near the surface (typically above the dotted line in Figure 3A), many distinct cavities and cracks amidst the hepatocytes are observed. In contrast, the deeper region has fewer such distinct vacant structures, but does exhibit thin threads between hepatocytes which likely correspond to hepatic sinusoids and normal capillary structures [17, 18]. The cause of the change in the superficial layer morphology may have been the freezing and thawing processes, with heterogeneous tissue alterations more prevalent near the unprotected top surface. Regardless of whether this morphology is caused by the tissue preparation/handling protocol, or is indicative of real rat liver microstructure, this resultant heterogeneity is reflected in the parametric α-maps obtained by the K-distribution fits. The biological features that do exist deeper (below the 150 μm line), such as portions of portal and hepatic vein structures marked by arrows on histology, are also seen on Figure 3B (albeit with lower resolution owing to the averaging process inherent in 3D α-map analysis). Importantly, neither the top layer heterogeneity nor the deeper venous structures are noticeable on the direct OCT structural image of Figure 2A.

In terms of quantification of these parametric liver tissue images, we observe that in the homogeneous hepatocyte region, α ~ 8, which yields N_{eff} ~ 4. The size of rat hepatocytes is ~20 μm, which is comparable to/slightly larger than dimensions of the coherence volume *V*. Thus, a simple interpretation with one hepatic cell equal to one scattering event is unlikely, suggesting subcellular organelles or extracellular matrix features are contributing to the light scattering signal [19]. The link between the volumetric crack density as seen on histology and our OCT-derived value of *N* ~ α/2 is unlikely to be direct. Rather, given the large number of cracks visualized histologically and the possibility of several effective 'scatterers' per crack (as these are not ideally flat in 3D, thus there may well be several scattering events at each shape irregularity/interface roughness), our determined *N*-value of >10 within the coherence volume of ~(12 μm)^3 in the superficial liver layers appears reasonable. Furthermore, direct characterization of refractive index variation can be an another approach to interpret N_{eff} [20]. The refractive index correlation function provides

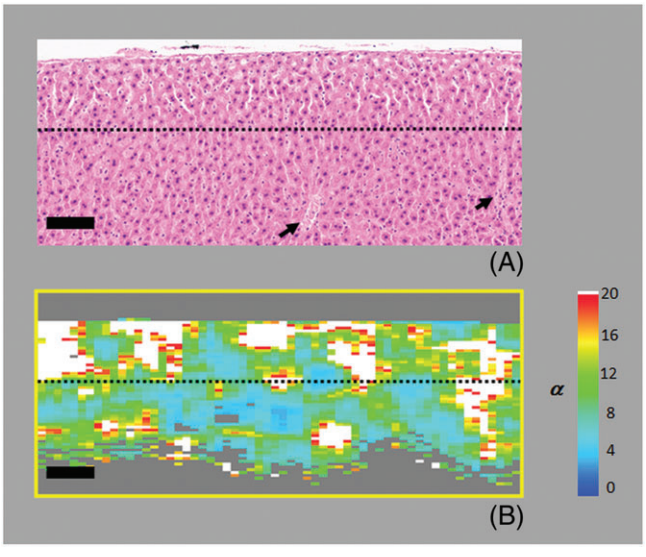

FIGURE 3 Histology of rat liver sample and comparison with the OCT α-map. (A) hemotoxylin and eosin section, with arrows indicating portal vein and hepatic venule branches. (B) Corresponding B-mode α-map (reproduced from Figure 2(E)). Scale bars: 100 μm. Histologically, superficial tissues (approximately above the dotted line, drawn at the depth of 150 μm) exhibit greater microstructural heterogeneity; this is reflected in the correspondingly greater variations in the parametric α-map

correlation length as an effective measure of inter-scatterer distance, and can then be used to estimate the scatterer density [21].

Next, as an example of heterogeneous biological tissue containing biological features and structures, the results from the fixed rat brain sample are shown in Figure 4. The *en face* FOV was 1.5×1.5 mm^2 with 384×384 A-scans, including parts of corpus callosum (CC), subiculum (Sub)/cornu ammonis 1 (CA1) and dentate gyrus (DG) in the hippocampal formation [22]. As expected, the α-map values vary widely in different parts of the brain tissues.

The OCT intensity images on the left side of the figure, especially the C-mode *en face* tomographs in Figure 4B,C, exhibit distinct features of CC, Sub/CA1 and DG regions, as expected from rat brain anatomy [22]. Turning to the K-distribution analysis of the right side of Figure 4, we first note that the contours 1 and 2 in the B-scan of Figure 4D show significant heterogeneity and structure within Sub/CA1, while appearing featureless on the standard OCT intensity images (Figure 4A). For example, as seen in Figure 4D, at the depth of C_2 there is a distinct drop of α values (from >20 to ~10) in region 1, whereas high α values persist throughout the imaging depth in region 2. In the C-scans (Figure 4E,F), the contours 1 and 2 were thus drawn to mark the corresponding positions from the B-scan of Figure 4A. Indeed, they also show the disappearance of high α domains with depth in region 1 and their depth persistence in region 2; these trends are also evident in and around the extended arc-shaped high-α-region-containing contours 1 and 2.

For this OCT brain imaging analysis, the interpretation of the high-α domains can be obtained from rat neuroanatomical atlases [22–25]. Specifically, the top of the CA1 region is known to be connected to the Sub, which has a different and more homogeneous microstructure: its pyramidal cells are more sparsely distributed than those in CA1, and the stratum lacunosum-moleculare is the only dendrite structure in Sub compared to the four-layer structure in CA1 [25]. Therefore, such tissue microarchitecture with rather uniformly distributed smaller features can exhibit a large

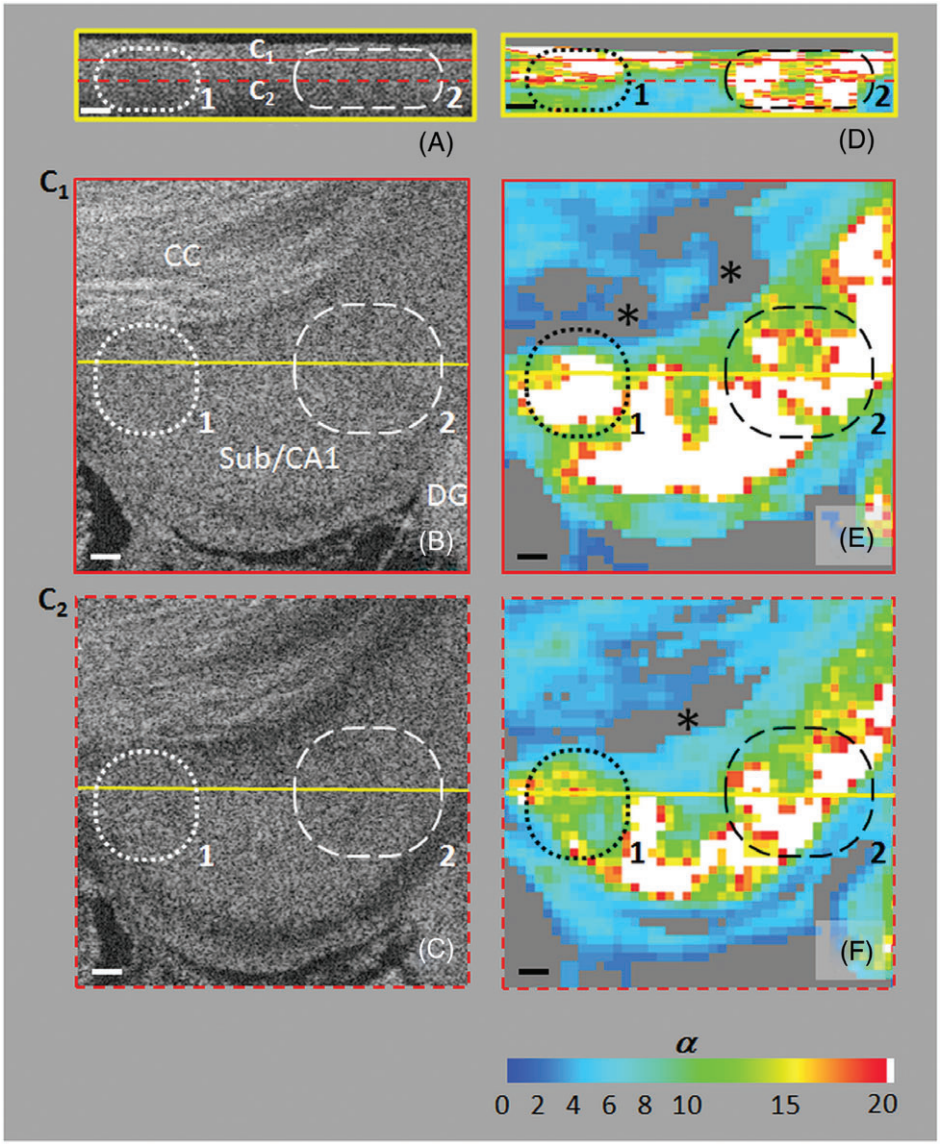

FIGURE 4 OCT intensity images (left side) and α-maps by K-distribution fit (right side) of a fixed rat brain. (A)–(C) B- and C-mode OCT intensity images showing corpus callosum (CC), subiculum (Sub), cornu ammonis 1 (CA1) and dentate gyrus (DG). (D)–(F) corresponding α-map. Grey areas indicates the exclusion of poor goodness-of-fit pixels that fall below the MSE > 3×10^{-7} threshold; asterisks show excluded area at the boundaries of CC and Sub/CA1. Scale bars: 100 μm. Contours 1 and 2 indicate regions within Sub/CA1 that contain various biological structures (derived from (A), see text for details); these are not evident on the OCT intensity images, but are clearly distinguishable in the α-maps

number of effective scatterers, and thus high α values, in the Sub region partly covering the CA1, as seen in Figure 4. Further, the other imaged brain section (results not shown) had retrosplenial and visual cortex regions on top of its field of view, and did not show correspondingly superficial high α layer—again this is consistent with what is anatomically known about the rat cortex microstructure [22–24, 26].

It should also be noted that tissue features with sufficient contrast differences and interfaces to be clearly visualized on OCT intensity images (eg, boundary of CC and Sub/CA1 in Figure 4B) are problematic for K-distribution PDF analysis. This is evident in the corresponding *en face* α-maps in Figure 4E,F, in which grey areas marked by asterisks indicate poor goodness-of-fit regions that fall below the MSE threshold (see Figure 2 and associated discussion). This is reminiscent of the distinct OCT intensity change seen in the liver sample (cf. very intense isolated spot in Figure 2D,G), which leads to large inhomogeneity within the α evaluation window. As the K-distribution fit to a single α value is not very meaningful for these boundary volumes containing two evidently different tissue regions, the exclusion of such pixels/voxels in the α-map is reasonable.

To summarize, parametric α-mapping analysis may be best suited for relatively homogenous tissue domains with subtle visibility features in which it may yield additional imaging contrast and information on underlying scatterer density. Conversely, this approach is not useful in regions of distinct boundaries that are directly visualizable through conventional OCT intensity contrast. Therefore, a complementary role and careful interpretation of parametric α-mapping analysis in OCT imaging is envisioned.

4 | CONCLUSION

In this study, we have shown a first demonstration of α-mapping in biological tissue by K-distribution fitting with a 3D sliding evaluation window for OCT intensity PDFs. Considerations of the suitable size of this 3D evaluation window were also presented. In rat liver, a relatively homogeneous tissue, good α contrast for fine structural changes near the sample surface, not seen in the OCT intensity images, was obtained. In a heterogeneous biological setting exemplified by rat brain tissue with a variety of boundaries and microstructures, these distinct features limit the utility of the K-distibution-fitting approach; nevertheless, regions of apparent OCT structural homogeneity were seen to correctly reflect the underlying brain anatomy on the derived α-maps. Further, interpretation of this novel contrast mechanism and its link to the effective number of scatterers within the coherence volume ($N_{\text{eff}} \sim \alpha/2$), directly and in the context of the refractive index variation in biological tissues, is a promising research direction currently pursued in our laboratory.

ACKNOWLEDGMENTS

The authors thank Dr Kostadinka Bizheva for her assistance with the OCT instrumentation. This study was supported by the Canadian Institutes of Health Research (grant no. 126172), the Ministry of Education and Science of the Russian Federation (14.B25.31.0015) and the Natural Sciences and Engineering Research Council of Canada/Canadian Institutes of Health Research through the Collaborative Health Research Program (J365581-09).

AUTHOR BIOGRAPHIES

Please see Supporting Information online.

REFERENCES

[1] E. Jakeman, R. J. A. Tough, *Adv. Phys.* **1988**, *37*, 471.
[2] E. Jakeman, P. N. Pusey, *IEEE Trans. Antenn. Propag.* **1976**, *24*, 806.
[3] E. Jakeman, P. N. Pusey, *Phys. Rev. Lett.* **1978**, *40*, 546.
[4] K. D. Ward, *Electron. Lett.* **1981**, *17*, 561.
[5] G. Parry, P. N. Pusey, *J. Opt. Soc. Am.* **1979**, *69*, 796.
[6] I. A. Popov, N. V. Sidorovsky, L. M. Veselov, *Opt. Commun.* **1993**, *97*, 304.
[7] A. Weatherbee, M. Sugita, K. Bizheva, I. Popov, A. Vitkin, *Opt. Lett.* **2016**, *41*, 2727.
[8] M. Sugita, A. Weatherbee, K. Bizheva, I. Popov, A. Vitkin, *Biomed. Opt. Express* **2016**, *7*, 2551.
[9] B. Davoudi, A. Lindenmaier, B. A. Standish, G. Allo, K. Bizheva, A. Vitkin, *Biomed. Opt. Express* **2012**, *3*, 826.
[10] D. W. Schaefer, *Science* **1973**, *180*, 1293.
[11] N. Weiss, T. G. van Leeuwen, J. Kalkman, *Phys. Rev. E* **2013**, *88*, 042312.
[12] S. H. Yun, G. J. Tearney, J. F. de Boer, B. E. Bouma, *Opt. Express* **2004**, *12*, 2977.
[13] J. Schmitt, A. Knüttel, *J. Opt. Soc. Am A* **1997**, *14*, 1231.
[14] M. Gu, C. J. R. Sheppard, X. Gan, *J. Opt. Soc. Am. A* **1991**, *8*, 1755.
[15] M. Muller, *Introduction to Confocal Fluorescence Microscopy*, 2nd ed., SPIE Press, Bellingham, WA **2006**.
[16] G. Lamouche, C.-E. Bisaillon, S. Vergnole, J. P. Monchalin, *Proc SPIE* **2008**, *6847*, 684724.
[17] J. Wilkinson, in *Medical Sciences*, 2nd ed. (Eds: J. Naish, D. Syndercombe-Court), Saunders Elsevier, Philadelphia **2014**, Ch. 15.
[18] M. Krishna, *Clinical Liver Disease* **2013**, *2*(S1), S4.
[19] J. M. Schmitt, G. Kumar, *Appl. Opt.* **1998**, *37*, 2788.
[20] J. M. Schmitt, G. Kumar, *Opt. Lett.* **1996**, *21*, 1310.
[21] M. Sugita, I. Popov, and A. Vitkin, **2017**, manuscript in preparation.
[22] D. Johnston, D. G. Amaral, in *The Synaptic Organization of the Brain*, 5th ed. (Ed: G. M. Shepherd), Oxford University Press, New York **2004**, Ch. 11.
[23] R. Bakker, P. Tiesinga, R. Kötter, *Neuroinformatics* **2015**, *13*(3), 353.
[24] E. A. Papp, T. B. Leergaard, E. Calabrese, G. A. Johonson, J. G. Bjaalie, *Neuroimage* **2014**, *97*, 374.
[25] R. Miettinen, T. Hajszan, A. Riedel, K. Szigeti-Buck, C. Leranth, *J. Neuroscience Methods* **2012**, *205*, 130.
[26] M. T. K. Kirkcaldie, T. C. Dickson, C. E. King, D. Grasby, B. M. Riederer, J. C. Vickers, *J. Chemical Neuroanatomy* **2002**, *24*, 163.

How to cite this article: Sugita M, Brown RA, Popov I, Vitkin A. K-distribution three-dimensional mapping of biological tissues in optical coherence tomography. *J. Biophotonics.* 2018;11:e201700055. https://doi.org/10.1002/jbio.201700055